

# Multiparameter Uncertainty Mapping in Quantitative Molecular MRI using a Physics-Structured Variational Autoencoder (PS-VAE)

Alex Finkelstein, Ron Moneta, Or Zohar, Michal Rivlin, Moritz Zaiss, Dinora Friedmann Morvinski, and Or Perlman, *Member, IEEE*

**Abstract**—Quantitative imaging methods, such as magnetic resonance fingerprinting (MRF), aim to extract interpretable pathophysiology biomarkers by estimating biophysical tissue parameters from signal evolutions. However, the pattern-matching algorithms or neural networks used in such inverse problems often lack principled uncertainty quantification, which limits the trustworthiness and transparency, required for clinical acceptance. Here, we describe a physics-structured variational autoencoder (PS-VAE) designed for rapid extraction of voxelwise multi-parameter posterior distributions. Our approach integrates a differentiable spin physics simulator with self-supervised learning, and provides a full covariance that captures the inter-parameter correlations of the latent biophysical space. The method was validated in a multi-proton pool chemical exchange saturation transfer (CEST) and semisolid magnetization transfer (MT) molecular MRF study, across in-vitro phantoms, tumor-bearing mice, healthy human volunteers, and a subject with glioblastoma. The resulting multiparametric posteriors are in good agreement with those calculated using a brute-force Bayesian analysis, while providing an orders-of-magnitude acceleration in whole brain quantification. In addition, we demonstrate how monitoring the multi-parameter posterior dynamics across progressively acquired signals provides practical insights for protocol optimization and may facilitate real-time adaptive acquisition. The code will be made publicly available upon acceptance.

**Index Terms**—Uncertainty Quantification, Molecular Imaging, Magnetic Resonance Fingerprinting (MRF), Chemical Exchange Saturation Transfer (CEST), Magnetization Transfer (MT), Self Supervised Learning, Quantitative MRI (qMRI).

## I. INTRODUCTION

SATURATION transfer magnetic resonance imaging (ST-MRI) is an increasingly investigated molecular imaging technique [1] that has already provided biological insights across a variety of preclinical [2]–[5] and clinical [6]–[8] applications. ST mechanisms comprise several contrast pathways, including chemical exchange saturation transfer (CEST), relayed nuclear Overhauser enhancement (rNOE), and semisolid magnetization transfer (MT) [1].

The CEST-weighted contrast reflects the combination of the proton volume fraction and exchange rate, and is influenced by a variety of confounding factors [9], including water relaxivity,

A.F., M.R., and O.P. are with the School of Biomedical Engineering, Tel-Aviv University, Tel-Aviv, Israel. O.Z. and D.F.M. are with the School of Biochemistry, Neurobiology, and Biophysics, Tel-Aviv University, Tel-Aviv, Israel. M.Z. is with the Institute of Neuroradiology, University Hospital Erlangen, and the Department of Artificial Intelligence in Biomedical Engineering, Friedrich-Alexander Universität Erlangen-Nürnberg (FAU), Erlangen, Germany. D.F.M., R.M., and O.P. are also with the Sagol School of Neuroscience, Tel-Aviv University, Tel-Aviv, Israel. e-mail: orperlman@tauex.tau.ac.il

direct water saturation, aliphatic rNOE, and macromolecule-associated signals. As for many other MRI contrast mechanisms, these dynamics have motivated the pursuit of a fully quantitative method, capable of isolating and mapping the biophysical parameters of interest.

In consequence, quantitative CEST studies have gradually shifted focus from traditional steady-state signal model fitting [10], [11], to quasi-steady-state [12], and pseudo-random acquisition patterns [13] that enable a shorter acquisition time. Two emerging technologies that play a key role in these endeavors are magnetic resonance fingerprinting (MRF) [14]–[18], and AI-based quantification [19]–[21].

Unfortunately, applying these techniques clinically is still hindered by (i) the absence of ground truth *in vivo*, (ii) the black-box nature of the deep learning models used to date, and (iii) the substantial variability in the biophysical parameter estimates obtained by different algorithmic variants and research groups [16], [20], [22]–[24]. It is therefore essential to characterize the uncertainties and biases of each estimated parameter pixel-wise, to foster trust in the AI-based quantitative imaging pipeline.

Our goal was to develop a rapid computational method to assess the joint uncertainties of quantitative MRI parameter estimates, by approximating the full posterior within a real-time neural-network-based quantification framework. The method was validated across various quantitative molecular (ST) MRI tasks, where the lack of appropriate multi-parameter uncertainty estimates constitutes an urgent need; however, the same concept can be applied for a variety of other quantitative imaging contrasts.

## A. Related Work

The standard formalization of seeking uncertainty-aware solutions of inverse problems such as MRI reconstruction and quantification is the Bayesian posterior estimation. The poor scaling of non-parametric approaches motivated functional approximations known as variational inference (VI) [25] or variational Bayes (VB) [26], [27]. The variational autoencoder (VAE) [28] provided further scaling via data-driven *amortization*, altering the inference stage from solving a per-observation optimization problem to a single forward pass of a shared neural network (NN). A separate line of work augmenting generic auto-encoding (AE) focuses on guidance by biophysical modeling. This recent concept concerns physics-informed self-supervised learning [20], [29]–[31], where the

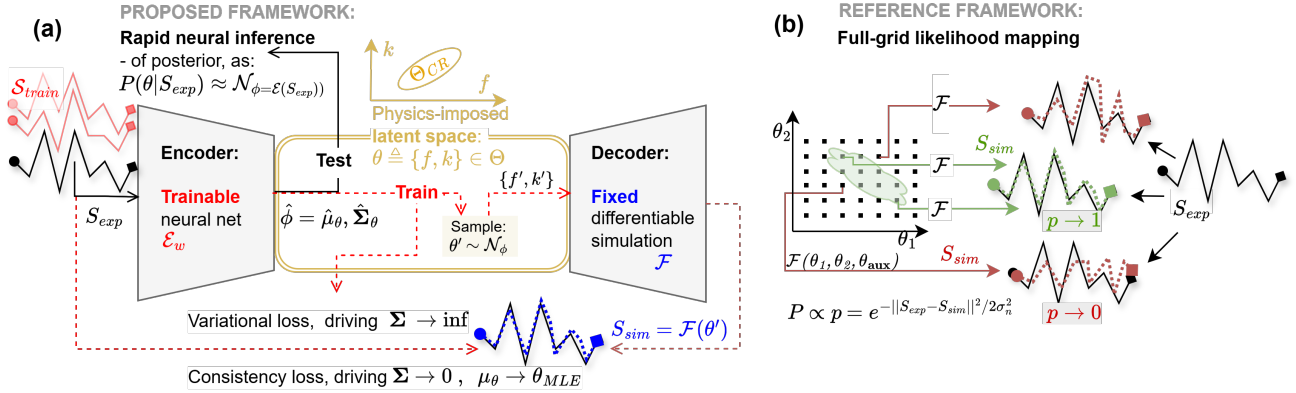


Fig. 1. Computational pipelines for multi-parameter posterior estimation in quantitative molecular MRI. (a) Rapid uncertainty estimation using a physics-structured variational autoencoder (PS-VAE). A multi-layer perception ( $\mathcal{E}_w$ , red) is trained using self-supervised learning on experimental signals  $S_{exp} \in \mathcal{S}_{train}$ . At inference, voxelwise parameterization  $\hat{\phi}(S_{exp}, w) = \hat{\mu}, \hat{\Sigma} = \mathcal{E}_w(S_m)$  of an approximate posterior  $\hat{P}(\theta|S_{exp}) \approx Q_{\hat{\phi}} = \mathcal{N}(\hat{\mu}, \hat{\Sigma})$  is obtained. The derived confidence region (CR)  $\Theta_{CR} \subset \Theta$  in the latent space of the tissue parameters  $\Theta$ , reflects consistency with the measured signal under a biophysical model ( $\mathcal{F}$ , blue), so that  $\mathcal{F}(\theta' \in \Theta_{CR}) \approx S_{exp}$ . The CR is an oriented uncertainty ellipsoid around the mean estimate  $\hat{\mu}$ , represented using a non-diagonal covariance matrix  $\hat{\Sigma}$ . A random posterior sample  $\theta' \sim Q_{\hat{\phi}}$  is decoded at each iteration during training, and a  $\Sigma$ -regularizing term balances the cycle-consistency loss. (b) Reference framework for likelihood-mapping. Each experimental signal  $S_{exp}$ , associated with a given voxel, is compared (by means of dot-product) to a local dictionary of signals across a dense grid in the parameter space  $\Theta = \Theta_1 \times \Theta_2$ . The discrepancy map is then translated into a likelihood and, consequently, into the posterior.

AE latent is associated with the point estimate of the physical parameters. This estimate is decoded by simulation into a ‘denoised’ output signal whose discrepancy with the experimental measurements then guides the training in order to improve the resilience to realistic signal distortions [20]. Here, we integrated these two approaches (probabilistic- and physics-driven AE extensions) within a simple yet meaningful multiparametric framework.

The concept of using a VAE over physics-grounded latent space has been explored in various contexts such as VAE-based perfusion MRI [32] and spatiotemporal modeling [33], [34] among others, with ref. [34] discussing applicability to uncertainty quantification (UQ) in inverse problems. However, these studies relied on synthetic datasets for training, incorporating heuristic assumptions on data and error distributions. In addition, previous VI methods apply the mean-field approximation, and neglect parameter correlations under the posterior, in seeking to predict a diagonal covariance matrix for the Gaussian approximation. Recent works extended VAE to use a full- or structured covariance, e.g. in the context of image formation and compressed sensing [35]. Similar ideas have been used to predict multivariate posteriors over dynamic contrast enhanced (DCE) MR parameters [36], but the reported training used synthetic data in a supervised learning fashion. Similarly, a related work in the CEST-weighted MRI field trained a NN to assess univariate uncertainties in a semi-quantitative parameter estimation task (accelerating standard Lorentzian fitting), without explicit posterior modeling [37].

Here, we introduce an amortized variational framework that explicitly captures the multivariate posterior structure within a self-supervised regime, enabling a rapid and robust probabilistic quantitative imaging.

## B. Main contributions

- Full-covariance quantification:* robust estimation of the joint posterior, capturing inter-parameter correlations.
- Physics-structured VAE architecture:* using the forward physical model as the decoder, we learn probabilistic inversion without synthetic data or ground-truth labels.
- Versatility:* robust performance across instance-specific and amortized VI modes: (i) fitting a single observation, and (ii) transfer to rapid inference on unseen subjects.
- Proof-of-concept applications:* (i) UQ-aware analysis and discovery of multiparameter biomarkers (ii) Posterior extraction from partial measurements, facilitating protocol optimization and real-time adaptive acquisition.

## II. METHODS

### A. Problem statement: Bayesian inversion of multi-pool MRI

and are directly affected by a variety of acquisition parameters, including the saturation pulse power ( $B_1$ ) and frequency offset ( $\Delta\omega$ ). For ST-MRF, the imaging scheme is repeated with pseudo-randomly varied saturation pulse parameters [17], essentially sampling the non-steady-state magnetization signal. The inverse problem of quantitative molecular MRI requires inferring the ODE coefficients from samples at different time points. Existing schemes for rapid NN-based parameter quantification can be formalized as a prediction of the maximum-likelihood point estimate (MLE) of biophysical parameters  $\theta$  from a measured signal  $S_m$ , under an assumed biophysical model  $\mathcal{F}$ , so that  $\mathcal{F}(\theta_{MLE}) \approx S_m$  [15]. Here, we extended this concept by approximating a Bayesian estimate of the joint posterior distribution  $P(\theta|S_m)$ . Furthermore, while classical MRF inherently relies on synthetic signals, we employ amortization over real (experimentally acquired) data, to avoid distribution shift concerns.

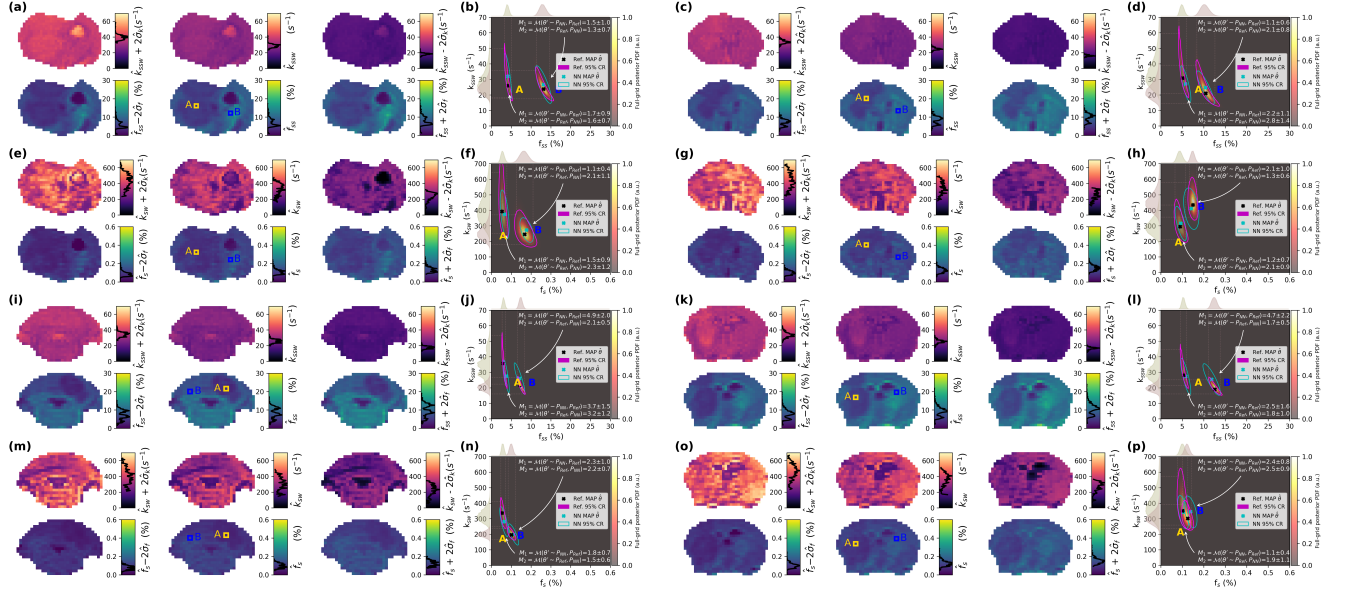


Fig. 2. **Uncertainty-aware quantification of the semisolid MT (a-d, i-l) and amide (e-h, m-p) proton exchange rates (top) and volume fractions (bottom) in tumor-bearing mice.** The color-coded brain images (a,c,e,g,i,k,m,o) show the PS-VAE output maps of maximum-a-posteriori (MAP) estimates of tissue parameters (center) and the corresponding univariate confidence interval (CI) bounds; the distributions across the entire slice are displayed inside the colorbar. Multi-parametric confidence regions (CR) are provided alongside each parameter map (b,d,f,h,j,l,n,p) for randomly chosen pixels in the ipsitumoral and contralateral regions of interest (ROIs), marked by "A" and "B" within the MAP images. The CRs were obtained from Gaussian posteriors using PS-VAE output (cyan) or from reference grid-based method (free-form CR bounds in magenta, underlying posteriors as heatmaps). The agreement between the two posteriors as quantified using the Mahalanobis distance is provided as text within the figure.

### B. Proposed framework: rapid quantification of the posterior

We extend the self-supervised architecture, interpreted as a physics-structured autoencoder (PS-AE) [20], to a variational version, termed PS-VAE (Fig. 1a). The true distribution  $P(\theta|S_m)$  is approximated by (i) designing the NN encoder to specify a member  $\phi$  of a Gaussian parametric family  $Q_\phi = \mathcal{N}(\mu, \Sigma)$ , (ii) sampling to back-propagate through probabilistic prediction ("reparameterization trick" [28]), and (iii) adding a regularizing term that balances the consistency loss. In contrast to vanilla VAEs, we impose a fixed decoder using the biophysical model  $\mathcal{F}$ , which aligns the latent space to that of the tissue parameters  $\theta \in \Theta$ . Distribution flexibility is provided by predicting a complete (non-diagonal) covariance matrix  $\Sigma$ , corresponding to an "uncertainty ellipsoid" around the mean estimate  $\mu$ . The weights  $w$  of the multi-layer perceptron (MLP) encoder  $\mathcal{E}_w$  are learned in a self-supervised manner from a training set  $\mathcal{S}_{\text{train}}$  comprised of experimentally measured signals. For each raw signal  $S_m$ , the encoder outputs the mean vector  $\mu$  and the covariance matrix  $\Sigma$  for a multi-variate Gaussian, representing the posterior distribution of the latent tissue parameter vector  $\theta$ . The VAE-inspired learning objective aims at uncertainty-regularized fitting:

$$\min_w \mathbb{E}_{S_m \in \mathcal{S}_{\text{train}}, \theta' \sim \hat{Q}(S_m)} [\mathcal{L}_c(S_m, \theta') + \mathcal{L}_{\text{reg}}(\mu, \Sigma)], \quad (1)$$

where  $\hat{\phi} = \mu, \Sigma = \mathcal{E}_w(S_m)$ ,  $\theta' \sim Q_{\hat{\phi}} = \mathcal{N}(\mu, \Sigma)$  is a posterior sample per step. The first term is the consistency loss, penalizing the residual between the measured and simulated signals:

$$\mathcal{L}_c(S_m, \theta') = \|S_m - \mathcal{F}(\theta')\|_2^2 \quad (2)$$

where  $\mathcal{F}$  is the differentiable biophysics-based simulator. The second term is the VAE regularization, as informed by the Kullback-Leibler (KL) divergence of posterior from a prior - an origin-centered Gaussian in standard VAEs, towards an analytical form:  $L_{KL} = \sum_j (\mu_j^2 + \sigma_j^2 - \log \sigma_j)$ , which in essence reflects a preference to  $\sigma$  of order of 1. Here, we employ a flat uniform prior across the physics-imposed latent space (within preset bounds) and adopt a simple heuristic, retaining the last term that prevents collapse of the uncertainty and adapting it for a full covariance as:

$$L_{\text{reg}} = -\alpha \log \det \Sigma = -\alpha \log \det \mathbf{S} = -\alpha \sum_j \log \lambda_j \quad (3)$$

where  $\alpha$  is a hyperparameter and the diagonal  $\mathbf{S} = \lambda \mathbf{I}$  refers to the result of the eigen-decomposition  $\Sigma = \mathbf{U} \mathbf{S}^2 \mathbf{U}^\top$ . The latter is also utilized in the re-parametrization trick sampling, for drawing  $\theta' \sim \mathcal{N}(\mu, \Sigma)$  from standard normal samples via:

$$\theta' = \mu + \mathbf{U} \mathbf{S} \epsilon, \quad \epsilon \sim \mathcal{N}(\mathbf{0}, \mathbf{I}_d), \quad (4)$$

In practice, the non-redundant terms of diagonal  $\mathbf{S}$  and orthonormal  $\mathbf{U}$  matrices are drawn from the encoder output.

### C. Reference framework: likelihood mapping

In the absence of ground truth for in vivo likelihood mapping, we provide a straightforward reference method that follows the true posterior as closely as possible. For a signal  $S_m$  at a given voxel, the Bayesian posterior is described by the likelihood and prior as:

$$P(\theta|S_m) = \frac{f(\theta)}{\int_{\theta' \in \Theta} f(\theta')}, \quad f(\theta) = P(\theta)P(S_m|\theta) \quad (5)$$

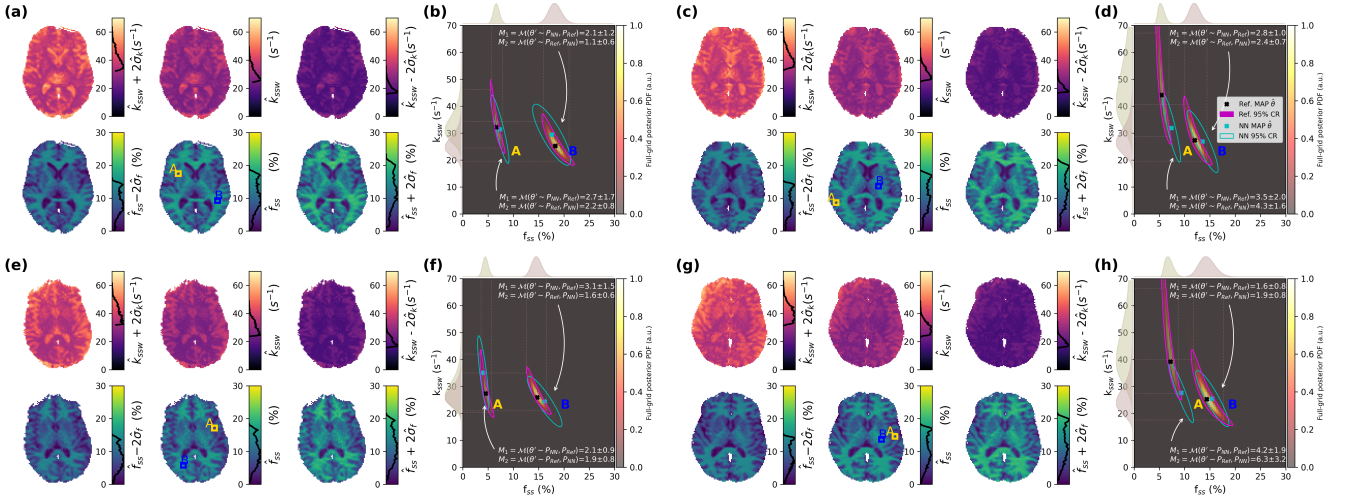


**Fig. 3. Uncertainty-aware quantification of the semisolid MT proton exchange rates (a,c,e,g, top) and volume fractions (a,c,e,g, bottom) in four healthy human volunteers.** The color-coded brain images show the PS-VAE output maps of maximum-a-posteriori (MAP) estimates of tissue parameters (center) and the corresponding univariate confidence interval (CI) bounds; the distributions across the entire slice are displayed inside the colorbar. Multi-parametric confidence regions (CR) are provided alongside each output parameter map (b,d,f,h) for randomly chosen pixels in the white and gray matter regions of interest (ROIs), as marked by "A" and "B" within the MAP images. The CRs were obtained from either Gaussian posteriors using the PS-VAE output (cyan) or a reference grid-based method (free-form CR bounds in magenta, underlying posteriors as heatmaps). The agreement between the two posteriors as quantified using the Mahalanobis distance is provided as text within the figure. The per-subject PS-VAE maps were obtained using a network trained on all other subjects (LOOCV, as described in section III-D).

The need to compute  $f(\theta)$  across the entire support  $\Theta$  for the denominator, typically discourages the use of this straightforward approach. However, for a low-dimensional case (e.g.,  $\theta \in \mathbb{R}^2$ ), a brute force computation across a reasonably detailed grid is both feasible (at least for a small number of voxels) and beneficial, for a transparent comparison. We assume the same biophysical model and an additive white Gaussian noise (AWGN) for the residuals of the  $n$  samples comprising the signal:

$$\mathbf{S}_m = (S^{(j)})_{j=1}^n \sim \mathcal{N}(\mathcal{F}(\theta_{true}, \theta_{aux}), \sigma_m \mathbf{I}_{n \times n}) \quad (6)$$

The accuracy can be improved by measuring auxiliary tissue parameters  $\theta_{aux}$  by independent imaging protocols whenever possible [16], [20]. Specifically,  $\theta_{aux} = \{T_1, T_2, B_0, B_1\}$  are used to improve the estimation of the semisolid magnetization transfer (MT) parameters  $\theta_{MT} = \{f_{ss}, k_{ssw}\}$ , and  $\{T_1, T_2, B_0, B_1, f_{ss}, k_{ssw}\}$  are subsequently used for the estimation of the amide proton transfer (APT) quantitative parameters  $\theta_{APT} = \{f_s, k_{sw}\}$ . We then simulate a dedicated dictionary of synthetic signals across a dense grid  $\Theta_d = \Delta\theta_1 \mathbb{Z} \times \Delta\theta_2 \mathbb{Z} \cap \Theta$  for a given  $S_m, \theta_{aux}$  at a voxel of interest:

$$\{S_{sim}(\theta) | \theta \in \Theta_d\} = \{\mathcal{F}(\theta_{1,2}, \theta_{aux}) | \theta_{1,2} \in \Delta\theta_{1,2} \mathbb{Z}_N\} \quad (7)$$

As the next step, the error model is plugged in for explicit computation of the likelihood map across the parameters grid:

$$P(S_m | \theta, \mathcal{F}, \sigma_{meas}) \propto e^{-\sum_{j=1}^n (\mathcal{F}(\theta)[j] - S_m[j])^2 / (2\sigma^2)} \quad (8)$$

The posterior is generated by multiplying the likelihood by a prior, and then normalizing to obtain a proper probability distribution function (PDF)  $P(\theta | S_m)$ .

#### D. Confidence region definition

The bi-variate 95% confidence regions (CRs) are defined for each estimation method, as the iso-posterior contours enclosing 95% of the probability density. For Gaussian posteriors (as provided by PS-VAE), the CRs reduce to Mahalanobis ellipses  $(\mathbf{x} - \mu)^\top \Sigma^{-1} (\mathbf{x} - \mu) = \chi^2_{2,0.95}$  (chi-square:  $\chi^2_{2,0.95} \approx 5.99$ ), with semi-axes  $a, b = \sqrt{\chi^2_{2,0.95} \lambda_{1,2}}$  and orientation  $\phi = \arctan(v_{1y}/v_{1x})$ , where  $\lambda_{1,2}$  and  $\mathbf{v}_{1,2}$  are the eigenvalues and the corresponding eigenvectors of  $\Sigma$  in descending order. The univariate confidence intervals (CIs) were similarly defined using marginalized posteriors; namely, using the  $\pm 2\sigma$  obtained from the diagonal of  $\Sigma$ , for the Gaussian case.

#### E. Evaluation criteria and performance metrics

1) *Goodness of fit for point estimates:* This criterion spatially maps the voxelwise fitting errors  $\|\mathcal{F}(\hat{\theta}) - S_m\|$  (as normalized mean squared error, NRMSE) of the neural network maximum a posteriori (MAP) estimate  $\hat{\theta} = (\hat{f}, \hat{k}) = \mu_\theta(S_m)$  compared to the value provided by the MAP estimate of the exact Bayesian  $\min(\|\mathcal{F}(\theta) - S_m\|) = \|\mathcal{F}(\theta_{MAP}) - S_m\|$ . In addition to reflecting the consistency between the raw experimental data and the model-based "re-synthesized" signals, this criterion also provides a rough estimate of model uncertainty.

2) *Univariate confidence interval (CI) accuracy:* The crude agreement of the UQ-aware univariate estimates as made by PS-VAE and the reference method was quantified as the percentage of pixels with any intersection between the parameter CIs provided by the two methods.

3) *Rigorous quantification of the multi-parameter posterior agreement:* The ability to capture the non-trivial joint parameter distributions was evaluated by using the 2-D Mahalanobis

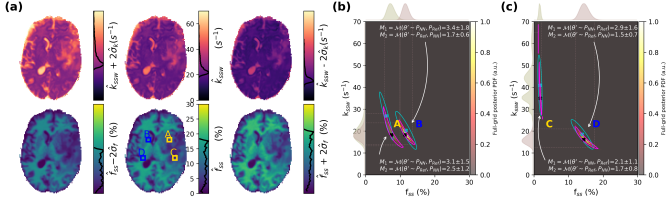


Fig. 4. **Uncertainty-aware quantification of the semisolid MT proton exchange rates (a, top) and volume fractions (a, bottom) in a patient with glioblastoma.** The color-coded brain images represent the PS-VAE output maps of maximum-a-posteriori (MAP) estimates of tissue parameters (center) and the corresponding univariate confidence interval (CI) bounds; the distributions across the entire slice are displayed inside the colorbar. Multi-parametric confidence regions (CR) are provided in (b,c) for randomly chosen pixels in the ipsitumoral and contralateral regions of interest (ROIs), marked by 'A', 'B', 'C', and 'D' within the MAP images. The CRs were obtained from Gaussian posteriors using the PS-VAE output (cyan) or from a reference grid-based method (free-form CR bounds in magenta, underlying posteriors as heatmaps). The agreement between the two posteriors as quantified using the Mahalanobis distance is provided as text within the figure.

distance  $\mathcal{M}(\theta, \mathcal{D})$  to compare the posteriors obtained by PS-VAE and by full-grid likelihood-mapping. The metric was calculated in a two-directional manner, namely as distances between samples from the distribution  $P_1(\theta|s)$  provided by one method to distribution  $P_2(\theta|s)$  provided by the other, and vice versa:  $\{\mathcal{M}(\theta', P_1)|\theta' \sim P_2\}, \{\mathcal{M}(\theta', P_2)|\theta' \sim P_1\}$ . The empirical distribution of these values was then compared to the ideal PDF curve of the Mahalanobis distances between samples and the distribution from which they had been drawn  $\mathcal{M}(\theta_{[\sim P]}, P) \sim \chi_{d=2}$  (with equality achieved at  $P_1 = P_2$ ). A threshold of  $M=4$  was determined as a "marginal agreement", heuristically extending the CI-intersection criterion  $\theta^{(1)} + 2\sigma^{(1)} > \theta^{(2)} - 2\sigma^{(2)}$  to a multivariate similarity.

### III. EXPERIMENTS

#### A. Datasets

1) *L-arginine (L-arg) phantoms at 9.4 T*: Open access data from an in-vitro MRF study in L-arg phantoms was used (<https://doi.org/10.6084/m9.figshare.2328980>) [38]. The phantoms consisted of three glass vials containing 50 mM L-arg with the pH titrated to 5.0, 5.5, and 6.0.

2) *Tumor-bearing mice at 7T*: All experimental protocols adhered to the ethical principles of the Israel National Research Council (NRC) and received approval from the Tel Aviv University Institutional Animal Care and Use Committee (IACUC). Two cell lines (O1, a cell line derived from a lentiviral-induced pediatric glioma [39], and GP01, a murine diffuse midline glioma primary tumor cell line [40]) were used to establish tumor mouse models in seven mice. All the mice were imaged using a 7T scanner (Bruker, Germany).

3) *Healthy human volunteers at 3T*: Four healthy volunteers (three females/one male, with an average age of  $23.75 \pm 0.83$ ) were scanned at Tel Aviv University using a 3T MRI (Prisma, Siemens Healthineers). The research protocol was approved by the TAU Institutional Ethics Board (study no. 2640007572-2) and the Chaim Sheba Medical Center Ethics Committee (0621-23-SMC).

4) *A subject with brain cancer at 3T*: A patient with glioblastoma was scanned with a 3T MRI (Prisma, Siemens Healthineers) at the University Hospital Erlangen (FAU) [41], using the same imaging protocol as for healthy volunteers. The research protocol was approved by the University Hospital Erlangen Institutional Review Board and Ethics Committee. The participant provided written, informed consent before the study.

#### B. MRI acquisition protocols

A continuous-wave (CW) MRF protocol with a single-slice spin-echo echo-planar-imaging (SE-EPI) readout was used for both phantoms and mice, with a saturation pulse frequency offset fixed at 3 ppm (phantoms), 3.5 ppm (APT imaging), or varied between 6-14 ppm (semisolid MT imaging) [15], [16].  $T_1$ ,  $T_2$ ,  $B_0$ , and  $B_1$  maps were acquired using rapid acquisition with relaxation enhancement (RARE), multi-echo spin-echo (MSME), water saturation shift referencing (WASSR) [42], and the double angle protocols, respectively. The field of view (FOV) was set to  $32 \times 32$  mm /  $19 \times 19$  mm and the slice thickness to 5 mm / 1.5 mm for phantoms/mice, respectively. The matrix size was set to 64 x 64 pixels for both phantoms and mice. For humans,  $T_1$ ,  $T_2$ ,  $B_0$ , and  $B_1$  maps were obtained using saturation recovery, multi-echo, and the WASABI [43] sequences, respectively. All human protocols used a 3D snapshot readout with whole-brain coverage [44] and an isotropic resolution of 1.8 mm [20]. A spin-lock saturation train ( $13 \times 100$  ms, 50% duty-cycle) was used for ST. The complete sequence definitions are listed in [17].

#### C. Computational framework implementation details

The framework was implemented in JAX [45] on a desktop computer equipped with an NVIDIA GeForce RTX 3060 GPU. A simple voxelwise multi-layer perceptron (MLP) with two hidden layers of 256 neurons each has been employed as the PS-VAE encoder. The training used batches comprised of 10/1 image slices, a learning rate of 0.001/0.01, and 350/1000 epochs, for the clinical or preclinical imaging, respectively. Complete code and sample data will be made publicly available upon acceptance.

#### D. Operating modes and evaluation procedures

a) *Rapid Bayesian quantification of unseen data*: Applying the PS-VAE-trained rapid neural posterior estimator to held-out data is referred to as *transfer mode* and seen as a manifestation of *amortized VI*. This has been evaluated on semisolid MT data from healthy volunteers, using a leave-one-out cross-validation (LOOCV) routine: training was performed on  $n-1=3$  subjects (using a total of 135 slices) and tested on the held-out data from the  $n^{th}$  subject. The process was repeated across all  $n=4$  split options.

b) *Small-data training*: The single-subject training and testing of PS-VAE is referred to as *fitting mode*, and seen as an *instance-specific VI*. This mode was applied to all phantom and mouse data, as well as to the single human cancer patient.

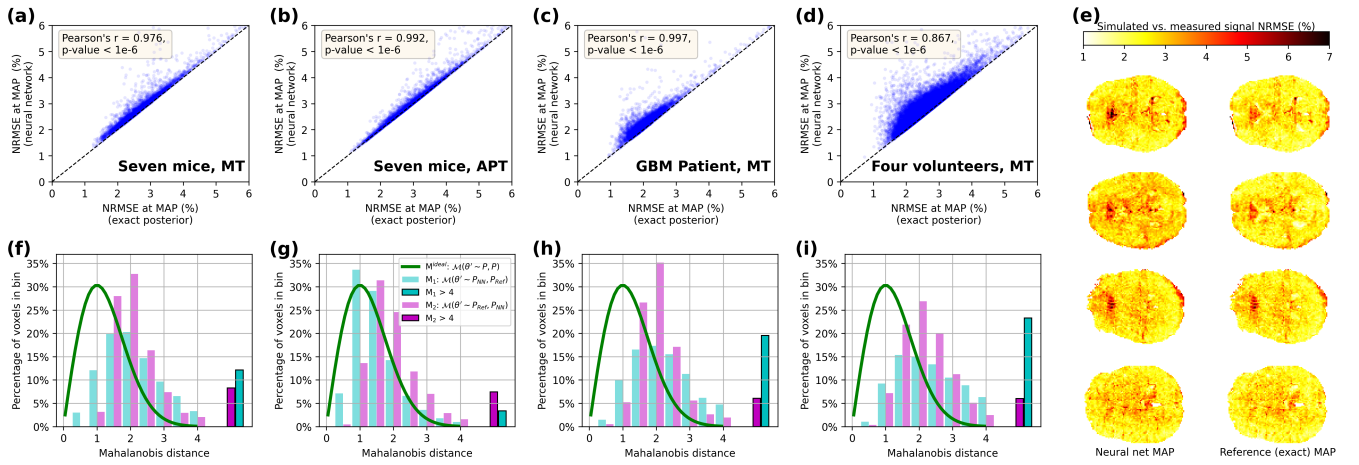


Fig. 5. Quantitative performance evaluation and statistical overview of the PS-VAE-derived output with respect to the reference method. (a-d). Correlation plots comparing the NRMSE (reflecting the goodness of fit) of the MAP parameter values obtained by PS-VAE (y-axis) and the reference exact Bayesian quantification method (x-axis), for all voxels of quantification of semisolid MT in mice (a), APT in mice (b), semisolid MT in a patient with glioblastoma (c), and in healthy volunteers (d). (e). NRMSE maps for PS-VAE-derived MAP values across four healthy volunteers. (f-i). Complete distribution of the Mahalanobis distances of samples from PS-VAE-derived posteriors to the reference posteriors (and vice-versa), aggregated from all voxels, for semisolid MT in mice (f), APT in mice (g), semisolid MT in a subject with glioblastoma (h), and in healthy volunteers (i). The ideal distribution (Mahalanobis distances of samples from any distribution  $P$  to same  $P$ ) is shown by the green curve in (f-i), for comparison.

TABLE I  
PERFORMANCE EVALUATION

Metric / target & setup	TB mice (n=7) APT 7T CW	TB mice (n=7) ssMT 7T CW	Healthy humans (n=4) ssMT 3T PW	GBM patient (n=1) ssMT 3T PW	Phantom (n=3 vials) L-arginine 9.4T CW
NRMSE for MAP values ("goodness of fit")	NN: $3.3\% \pm 0.7\%$ Ref: $3.2\% \pm 0.6\%$	NN: $3.0\% \pm 0.3\%$ Ref: $2.8\% \pm 0.3\%$	NN: $2.9\% \pm 0.1\%$ Ref: $2.6\% \pm 0.1\%$	NN: 2.5% Ref: 2.3%	NN: $2.2\% \pm 0.0\%$ Ref: $2.1\% \pm 0.0\%$
Univariate CIs intersect (percentage of voxels)	$f_{ss}$ : $99.9\% \pm 0.1\%$ $k_{ssw}$ : $99.6\% \pm 0.4\%$	$f_{ss}$ : $99.4\% \pm 0.4\%$ $k_{ssw}$ : $98.1\% \pm 1.2\%$	$f_{ss}$ : $98.7\% \pm 0.5\%$ $k_{ssw}$ : $97.2\% \pm 1.1\%$	$f_{ss}$ : 98.4% $k_{ssw}$ : 96.7%	$f_{ss}$ : $100.0\% \pm 0.0\%$ $k_{ssw}$ : $100.0\% \pm 0.0\%$
Mahalanobis distance (median across all voxels)	$M_1 = 1.39 \pm 0.14$ $M_2 = 1.86 \pm 0.20$	$M_1 = 2.17 \pm 0.4$ $M_2 = 2.02 \pm 0.10$	$M_1 = 2.57 \pm 0.67$ $M_2 = 2.09 \pm 0.32$	$M_1 = 2.39$ $M_2 = 1.99$	$M_1 = 2.14\% \pm 0.39\%$ $M_2 = 1.59\% \pm 0.41\%$
Posteriors discrepancy (percentage of voxels)	$M_1 > 4$ : $3.2\% \pm 1.0\%$ $M_2 > 4$ : $7.9\% \pm 4.9\%$	$M_1 > 4$ : $12.9\% \pm 5.3\%$ $M_2 > 4$ : $8.3\% \pm 3.2\%$	$M_1 > 4$ : $20.8\% \pm 12.1\%$ $M_2 > 4$ : $4.5\% \pm 0.8\%$	$M_1 > 4$ : 19.5% $M_2 > 4$ : 6.1%	$M_1 > 4$ : $2.1\% \pm 2.3\%$ $M_2 > 4$ : $0.2\% \pm 0.3\%$

TB: tumor-bearing; APT: amide proton transfer; ssMT: semisolid magnetization transfer; CW/PW: continuous/pulsed wave; GBM: glioblastoma multiforme.

## IV. RESULTS AND DISCUSSION

### A. Uncertainty visualization and biomedical interpretation

Representative univariate confidence interval (CI) maps for tumor-bearing mice, healthy human volunteers, and a patient with glioblastoma are shown in Figs. 2a,c,e,g,i,k,m,o, 3a,c,e,g, and 4a, respectively. The maps provide immediate visual insights into the reliability of each quantified tissue parameter, as opposed to a "stand-alone" observation of the MAP estimates ( $\hat{f}_{ss}$ ,  $\hat{f}_s$ ,  $\hat{k}_{ssw}$ ,  $\hat{k}_{sw}$ , center column in the above mentioned sub-figures). Specifically, the CI maps for the semisolid MT proton volume fraction ( $f_{ss}$ ) are relatively tight and narrowly distributed, due to the high concentration of semisolid macromolecules in the brain (especially in the white matter). In contrast, the CI maps for the semisolid proton exchange rate ( $k_{ssw}$ ) exhibit a substantially wider distribution, in agreement with previous reports attesting to the difficulty in accurately determining the value of this challenging physical property [13], [17], [46]. Similarly, the spatial CI maps of the amide proton exchange rate ( $k_{sw}$ , Fig. 2e,g,m,o) exhibit a wide uncertainty (large  $\sigma$ ), which may explain the wide variability

in previous reports [16], [20], [22]–[24].

While the univariate CIs represent the first layer of information, deeper insights are provided by the joint multi-parametric posteriors (Figs. 2b,d,f,h,j,l,n,p, 3b,d,f,h, and 4b,c). The eccentricity and inclination of the confidence regions in the semisolid MT quantification in mouse and human brains indicates a negative correlation between  $f_{ss}$  and  $k_{ssw}$  under the posterior. These findings are consistent with simplified analytical models where the leading-order behavior of the ST effect is proportional to the product of the proton volume fraction and exchange rate [1]. In addition they provide further evidence for the necessity of full covariance for approximating the exact CRs. The posterior maps provide a straightforward visualization of the multi-parameter differences across various tissue types; a glance at these maps for healthy human volunteers immediately conveys the differences in proton volume fraction and exchange rates between white and gray matter (WM/GM). These can be seen in the separation between the respective curvilinear CRs (mostly horizontal, namely better reflected by changes in  $f_{ss}$ ). The overlap of the two univariate PDFs obtained by marginalizing, i.e. projecting the posteriors

onto the proton volume fraction and exchange rate axes (Figs. 2b,d,f,h,j,l,n,p, 3b,d,f,h, and 4b,c) provides an alternative way to assess the discriminative power of a given biophysical parameter. Specifically, when analyzed at a single-pixel level (as shown in Figs. 2, 3, and 4), the CRs and their projection on the biophysical parameter axes can be used to determine whether an ipsilateral pixel is substantially different from the contralateral counterpart. For example, Fig. 2f shows that murine tumor edema consistently decreases the amide proton volume fraction [16], leading to non-overlapping projected PDFs for  $f_s$ . On the other hand, while the MAP for the ipsitumoral  $k_{sw}$  appears larger than the contralateral region for some mice (Fig. 2e), a careful look at the CR map reveals a non-negligible PDF tail overlap (Fig. 2f). This finding is in agreement with a recent 31P imaging study that reported a less than 0.1 pH units [47] increase in intracellular pH in the tumor (associated with the amide proton base catalyzed proton exchange rate increase). Unlike tumor proliferation, cell death is known to be associated with a substantial decrease in pH (and amide  $k_{sw}$ ). This is typically seen following successful cancer treatment [16], [48]. While our study did not involve treatment, the availability of the CR map may enable the determination of certainty for a more subtle form of cell death that is often seen in late tumor stages (Fig. 2g,h). Importantly, observing the posterior maps across different voxels further emphasizes the heterogeneity of the tissue parameter values for human glioblastoma (Fig. 4b,c), compared to the more homogeneous mouse tumor model (Fig. 2).

### B. Uncertainty quantification benchmarking

Table I presents a summary of method performance across various imaging targets, hardware, and setups. Notably, the subject-mean NRMSE representing the goodness of fit of the PS-VAE-derived point estimates are lower than 4% across all experiments. In addition, the NRMSE values obtained by the PS-VAE-derived MAP estimates are strongly correlated with those obtained by the reference method (Fig. 5a,  $r=0.976$ ,  $r=0.992$ ,  $r=0.867$ , and  $r=0.997$  for APT in mice, MT in mice, healthy volunteers, and a GBM patient, respectively, with  $p<0.001$  in all cases).

Basic agreement is also indicated by the overlap between the univariate CIs obtained by PS-VAE and those from the reference method seen in more than 95% of voxels in all the *in vivo* studies. A similarly good agreement is indicated by the two-directional Mahalanobis distances ( $M_1/M_2$ ) of the PS-VAE-derived and reference posteriors, with a median  $M<2.6$  across all imaging targets and setups (Table I). PS-VAE tended to produce wider CRs than the reference method in semisolid MT parameter quantification, as demonstrated by a typical  $M_2 \lesssim M_1$ . The  $M_2$ , which represents the expected divergence of 'true values' from the PS-VAE-provided CRs, was smaller than 4 in more than 91.7% of the voxels across all *in vivo* setups (95.5% for the healthy-human volunteers tested in transfer mode). The full distributions of the Mahalanobis distances, across the various imaging experiments are shown in Fig. 5f-i. Twenty-eight visual examples of posteriors alongside the corresponding Mahalanobis values are provided

for a variety of random GM/WM pixels (Fig. 3b,d,f,h) and tumor/contralateral pixels (Figs. 2b,d,f,h,j,l,n,p; 4b,c).

The rapid quantification of unseen data, using the PS-VAE-trained decoder, generated consistent MAP and CI maps (as part of the LOOCV study, Fig. 3) with a between-subjects coefficient-of-variance (CV) of:  $CV(f_{ss})=2.5\%/7.2\%$  and  $CV(k_{ssw})=2.2\%/2.3\%$ , for the WM/GM regions, respectively. At the same time, there was consistently good model data-fit, as shown in Fig. 5d,e.

### C. Computational performance

The PS-VAE training for the human 3D brain imaging analysis required  $9.5\pm0.1$  min., and the inference on a test subject 3D volume was completed in  $1.04\pm0.03$  s. This is in contrast to the  $1.6\pm0.5$  s for a single voxel and  $127.4\pm6.7$  min for a slice (projected to an average of 95.5 hours for the whole brain) required for the reference method (likelihood mapping using a  $100\times100$  grid for  $10^4$  parameter combinations). The fitting in mouse 2D imaging (MT+APT), required  $6.4\pm0.4$  min per mouse, compared to  $0.57\pm0.01$  s per voxel and  $10.0\pm1.3$  min for a whole slice required for likelihood mapping.

### D. Per-voxel Bayesian uncertainty vs. inter-voxel variation

There are certain pitfalls in applying complex neural networks to parameter-quantification tasks. These include hallucinations of anatomical structures, non-existing contrast, and smoothing. For example, even though we deliberately employed a simplistic network architecture (voxelwise MLP) to prevent anatomy and brain structure memorization, the NN-based point estimate (MAP) maps for  $k_{ssw}$  were still visibly smoothed (reflecting an implicit denoising prior [20]). Thus, a simplistic assessment of robustness based on MAP spatial noise may underestimate the true uncertainty in tissue parameter quantification when used with neural estimators. This again highlights the need for UQ. While Figs. 2, 3, and 4 present explicit maps of CI bounds, Fig. 6 represents a further alternative option for visualization, where maximum a posteriori (MAP) estimate maps are compared to a random sampling of voxelwise posteriors in a tumor-bearing mouse; **Supplementary Video 1** extends Fig. 6a-d to illustrate the variability across samples and subjects. Notably, the general agreement between the posterior-driven variations and the spatial-based variations provides meaningful validation of the basic assumptions. An exception was observed in the neural estimation of  $k_{ssw}$ , where the spatial noise appears suppressed (smoothed). However, sampling from the PS-VAE-based posteriors yielded a realistic restoration of the spatial variance (Fig. 6b, bottom), in line with the exact Bayesian reference (Fig. 6d, bottom). Therefore, UQ visualization via direct voxelwise projection of randomly sampled posteriors may serve as another way to mitigate the potential impact of NN biases on the clinical user's perception. Another implication of our findings, in the context of the search for a quantitative imaging biomarker (QIB) that can be used for tissue classification (e.g., tumor vs normal), relates to the desirability of a "single-number" value that represents the discrimination potential of a given biophysical parameter. Unfortunately, the traditional

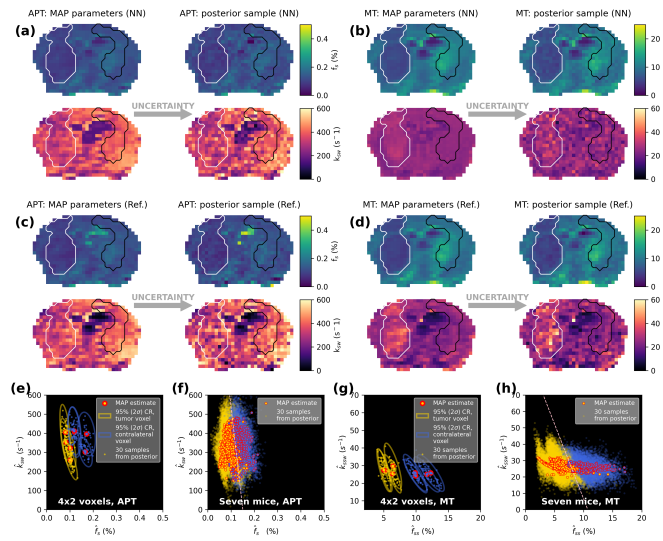


**Fig. 6. Posterior sampling as a means for mitigating denoising priors and evaluating multi-parameter biomarker potential.** (a,c) Quantitative amide proton volume fraction ( $f_s$ , top) and exchange rate ( $k_{ssw}$ , bottom) in a tumor-bearing mouse, obtained using PS-VAE-based point estimates (a, left), the reference method (c, left), and by random sampling of corresponding voxelwise posteriors (a,c, right). (b,d) Quantitative semisolid MT proton volume fraction ( $f_{ss}$ , top) and exchange rate ( $k_{ssw}$ , bottom) in the same mouse, obtained using PS-VAE-based point estimates (b, left), the reference method (d, left), and by random sampling of PS-VAE-based voxelwise posteriors (b,d, right). Tumor and contralateral ROIs (as used for voxel classes in e-h) are shown with white and black contours respectively. See **Supplementary Video 1** for an animated visualization of voxelwise posterior sampling variability across subjects. (e-h) Uncertainty-aware assessment of a multi-parametric quantitative biomarker potential. e,g. A demonstration of the posterior sampling concept across 8 voxels (color-coded by tissue type, 4 for each), showing the PS-VAE MAP estimates (red-circled points), the bounds of 95%-CRs obtained from the PS-VAE posteriors, and 30 individual samples per voxel (non-circled points) for APT (e) and semisolid MT (g). f,h. A UQ-informed linear tissue classifier (dashed white line) is obtained by training on data augmented by posterior sampling, following pixel aggregation from multiple subjects for APT (f) and semisolid MT (h) imaging. Note the agreement between methods as well as between spatial/posterior variation. The spatial-smoothing effect of neural estimation is seen for  $k_{ssw}$  (bottom b, g, h), and mitigated by the UQ-based sampling, which protects against over-confidence.

contrast-to-noise ratio (CNR) metric may be biased when maps are overly smoothed. As an alternative, we propose a probabilistically sound definition of a Contrast-to-total-Uncertainty-Ratio (CUR) for a parameter  $\theta_i$  by replacing the denominator calculation in the CNR expression with sampling from voxelwise multi-parametric posteriors  $P_{\theta}^{(v)}$ :

$$CUR(\theta_i, \mathcal{V}_1, \mathcal{V}_2) := (\mu_1 - \mu_2) / \sqrt{(V_1^{tot} + V_2^{tot}) / 2}$$

$$\mu_{1,2} = \left\langle \hat{\theta}_i^{(v)} \right\rangle_{v \in \mathcal{V}_{1,2}}; V_{1,2}^{tot} = \left\langle (\theta_i(v) - \mu_{1,2})^2 \right\rangle_{v \in \mathcal{V}_{1,2}} \quad (9)$$

$$\theta_i'(v) = (\theta \sim P_{\theta}^{(v)})[i]$$

where  $\mathcal{V}_{1,2}$  refer to the ROIs of two tissues. Employing this metric on all seven tumor-bearing mice used in this study yielded a CUR of  $1.93 \pm 0.50$ ,  $0.26 \pm 0.16$ ,  $1.23 \pm 0.41$ , and  $0.61 \pm 0.43$ , for  $f_{ss}$ ,  $k_{ssw}$ ,  $f_s$ , and  $k_{sw}$ , respectively, in line with the trend revealed by the certainty-based assessment described in section IV-A.

As shown earlier, PS-VAE inherently extends beyond univariate estimates and may facilitate UQ-aware multi-

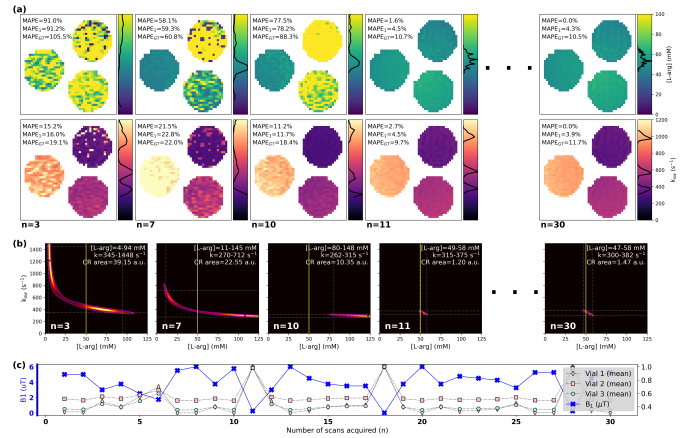


**Fig. 7. Continuous monitoring of multi-parameter posterior dynamics across progressively acquired CEST quantitative images in an L-arginine phantom.** (a) L-arginine concentration (top) and proton exchange rate ( $k_{ssw}$ , bottom) quantitative estimates, extracted using the dictionary best fit entry. The early-stopping error (as mean absolute percent error, MAPE) of partial-data estimate ( $\hat{\theta}[n]$ ,  $\theta := \{f_s, k_{ssw}\}$ ) compared voxelwise to the full-protocol (30 images) estimates  $\hat{\theta}[N]$  is presented for each dynamic image, alongside alternative comparisons: (i) to vial-mean of  $\hat{\theta}$  ( $MAPE_1$ ); (ii) to ground truth - known concentrations and proton exchange rate independently estimated using QUESP [15] ( $MAPE_{GT}$ ). (b) Bivariate confidence regions (CRs) for a random phantom voxel. (c) The saturation pulse powers used throughout the imaging protocol (the frequency offset was fixed at 3 ppm [15]); and the resulting signal values (averaged by vial, and normalized by maximal value).

parametric QIBs [49]. This is demonstrated in Fig. 6f,h, using a simplistic linear 'tissue-classifier', trained using posterior samples aggregated from all mice voxels. Interestingly, the slanted decision boundary in Fig. 6h assigned a role to  $k_{ssw}$  in classification, despite its low individual CUR. In other words, while univariate UQ indicates the limited potential of the  $k_{ssw}$  parameter as a self-contained tumor biomarker, the joint bivariate UQ suggests that it may still add value when combined with the semisolid MT proton volume fraction, as part of a multi-parametric QIB.

#### E. Adaptive acquisition by multi-parameter posterior tracking

The ability to quantify uncertainty rapidly opens new opportunities for online optimization of acquisition protocols, in a subject-specific manner. As a proof of concept, we retrospectively calculated the pixel-wise posteriors for progressively acquired experimental data (applying Eq. 8 with  $n' < n$ ), obtained using CEST (Fig. 7) or semisolid MT (Fig. 8) MRF protocols. Using the posteriors, we tracked CR shrinking as measurements accumulated (Fig. 8b,c and 7b) and used this as a surrogate for quantification accuracy. In other words, the CRs can serve as a direct means for (potentially) informing the MRI operator that the scan can be stopped and no additional data acquisition is needed. The Pearson's correlations between the CRs and the early-stopping error (aggregated as mean absolute percentage error, MAPE) were ( $r=0.77, p<0.001$ ) and ( $r=0.95, p<0.001$ ) for the  $f_{ss}$  and  $k_{ssw}$  estimation, respectively (Fig. 8e). Furthermore, the width of the CRs provided a tight bound for the quantification accuracy (Fig. 8f), as the de-facto errors of  $f_{ss}$  and  $k_{ssw}$  estimation due to early stopping were consistently smaller than the CR-based bound - in 96.5%

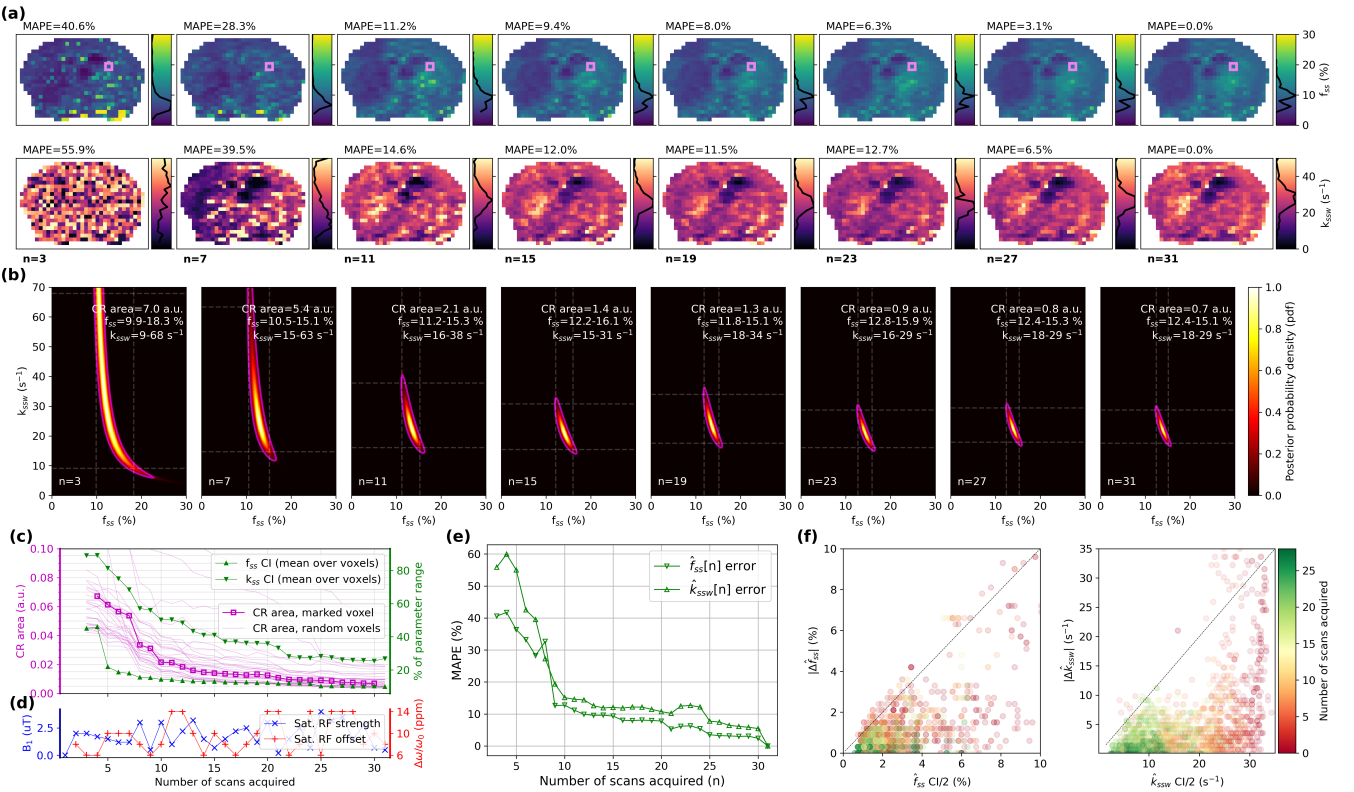


Fig. 8. Continuous monitoring of multi-parameter posterior dynamics across progressively acquired semisolid magnetization transfer (MT) quantitative images in a tumor-bearing mouse. (a) Semisolid MT proton volume fraction ( $f_{ss}$ , top) and exchange rate ( $k_{ssw}$ , bottom) quantitative estimates, extracted using the dictionary best fit entry. The retrospective early-stopping error ( $\Delta\theta_n = |\hat{\theta}(S_{[1, \dots, n < N]}) - \hat{\theta}(S_{[1, \dots, N]})|$ ;  $\theta \in \{f, k\}$ , aggregated over voxels as mean absolute percent error (MAPE):  $\Delta\theta/\theta (\%)$ ) is presented above each dynamic image. (b) Bivariate exact posteriors (heatmap) and confidence region (CR) bounds (magenta) derived by Eqs. 6-8, for a random brain voxel. (c) Calculated CR area and univariate 1D confidence interval (CI) widths (green) aggregated over brain voxels. (d) The saturation pulse power and frequency offset used throughout the imaging protocol. (e) The mean relative early-stopping error (MAPE, %) across partial sequence lengths (n). (f) A comparison between the estimated confidence interval semi-widths (CI/2) and retrospective early-stopping error ( $\Delta\theta$ ) across all brain voxels and  $n=1, 31$  acquired images (color-coded).

and 94.3% of the samples, respectively. In both animal and phantom studies, convergence to stable CRs/CIs, and, in turn, to a stable quantification error, occurred before 50% of the original sequence was completed, suggesting that substantial acceleration can be achieved with only a minor degradation in performance. The CR convergence rate was generally in line with the diversity of saturation pulse parameters offered by the acquisition protocol, as most intuitively shown at  $n=11$  for the phantom imaging case (Fig. 7c). Adding an additional measurement with a  $B_1$  distinctly different from previous measurements yielded improved encoding capability. This finding is consistent with previous protocol optimization reports [50] that relied solely on comparing quantification maps (Fig. 7a) with the final output (i.e., the full acquisition protocol length). In contrast, here we offer a roadmap to real-time adaptivity through CR-tracking (Fig. 7b).

## V. CONCLUSION

We have developed an uncertainty-aware physics-guided quantification framework that provides per-voxel confidence intervals and multivariate confidence region estimates in nearly real time. The results underscore the importance of characterizing joint uncertainty in quantitative molecular MRI. The PS-VAE methodology can be adapted for probabilistic

quantification in any imaging modality by simply switching the decoder's forward model, facilitating robustness and speed, critical requirements for clinical translation.

## REFERENCES

- [1] M. Zaiss *et al.*, “Theory of chemical exchange saturation transfer mri in the context of different magnetic fields,” *NMR in Biomedicine*, vol. 35, no. 11, p. e4789, 2022.
- [2] Z. Zhou *et al.*, “Optimized cest cardiovascular magnetic resonance for assessment of metabolic activity in the heart,” *Journal of cardiovascular magnetic resonance*, vol. 19, no. 1, p. 95, 2017.
- [3] P. Z. Sun *et al.*, “Detection of the ischemic penumbra using ph-weighted mri,” *J. of Cer. Blood Flow & Met.*, vol. 27, no. 6, pp. 1129–1136, 2007.
- [4] M. Rivlin, O. Perlman, and G. Navon, “Metabolic brain imaging with glucosamine cest mri: in vivo characterization and first insights,” *Scientific Reports*, vol. 13, no. 1, p. 22030, 2023.
- [5] K. Pavuluri *et al.*, “Noninvasive monitoring of chronic kidney disease using ph and perfusion imaging,” *Science advances*, vol. 5, no. 8, p. eaaw8357, 2019.
- [6] K. M. Jones, A. C. Pollard, and M. D. Pagel, “Clinical applications of chemical exchange saturation transfer (cest) mri,” *Journal of Magnetic Resonance Imaging*, vol. 47, no. 1, pp. 11–27, 2018.
- [7] J. Zhou *et al.*, “Review and consensus recommendations on clinical apt-weighted imaging approaches at 3t: application to brain tumors,” *Magnetic resonance in medicine*, vol. 88, no. 2, pp. 546–574, 2022.
- [8] E. Vinogradov *et al.*, “Cest-mri for body oncologic imaging: are we there yet?” *NMR in Biomedicine*, vol. 36, no. 6, p. e4906, 2023.
- [9] M. Zaiss and P. Bachert, “Chemical exchange saturation transfer (cest) and mr z-spectroscopy in vivo: a review of theoretical approaches and methods,” *Physics in Med. & Biology*, vol. 58, no. 22, p. R221, 2013.

[10] M. T. McMahon *et al.*, "Quantifying exchange rates in chemical exchange saturation transfer agents using the saturation time and saturation power dependencies of the magnetization transfer effect on the magnetic resonance imaging signal (QUEST and QUESP): pH calibration for poly-L-lysine and a starburst dendrimer," *Magnetic Resonance in Medicine*, vol. 55, no. 4, pp. 836–847, 2006.

[11] D. E. Woessner *et al.*, "Numerical solution of the Bloch equations provides insights into the optimum design of PARACEST agents for MRI," *Mag. Res. Med.*, vol. 53, no. 4, pp. 790–799, 2005.

[12] H. Kim, L. C. Krishnamurthy, and P. Z. Sun, "Demonstration of fast multi-slice quasi-steady-state chemical exchange saturation transfer (quass cest) human brain imaging at 3t," *Magnetic resonance in medicine*, vol. 87, no. 2, pp. 810–819, 2022.

[13] O. Perlman, C. T. Farrar, and H.-Y. Heo, "Mr fingerprinting for semisolid magnetization transfer and chemical exchange saturation transfer quantification," *NMR in Biomedicine*, vol. 36, no. 6, p. e4710, 2023.

[14] D. Ma *et al.*, "Magnetic resonance fingerprinting," *Nature*, vol. 495, no. 7440, pp. 187–192, 2013.

[15] O. Cohen *et al.*, "Rapid and quantitative chemical exchange saturation transfer (CEST) imaging with magnetic resonance fingerprinting (MRF)," *Magnetic Resonance in Medicine*, vol. 80, no. 6, 2018.

[16] O. Perlman *et al.*, "Quantitative imaging of apoptosis following oncolytic virotherapy by magnetic resonance fingerprinting aided by deep learning," *Nat. Biomed. Eng.*, vol. 6, no. 5, pp. 648–657, May 2022.

[17] N. Vladimirov *et al.*, "Quantitative molecular imaging using deep magnetic resonance fingerprinting," *Nature protocols*, pp. 1–31, 2025.

[18] I. Power *et al.*, "In vivo mapping of the chemical exchange relayed nuclear overhauser effect using deep magnetic resonance fingerprinting," *iScience*, vol. 27, no. 11, 2024.

[19] L. Chen *et al.*, "In vivo imaging of phosphocreatine with artificial neural networks," *Nature communications*, vol. 11, no. 1, p. 1072, 2020.

[20] A. Finkelstein *et al.*, "Multi-parameter molecular MRI quantification using physics-informed self-supervised learning," *Commun Phys*, vol. 8, no. 1, pp. 1–11, Apr. 2025.

[21] B. Kang *et al.*, "Unsupervised learning for magnetization transfer contrast mr fingerprinting: application to cest and nuclear overhauser enhancement imaging," *Magnetic resonance in medicine*, vol. 85, no. 4, pp. 2040–2054, 2021.

[22] D. Liu *et al.*, "Quantitative characterization of nuclear overhauser enhancement and amide proton transfer effects in the human brain at 7 Tesla," *Magnetic Resonance in Medicine*, vol. 70, no. 4, 2013.

[23] H. Y. Heo *et al.*, "Quantifying amide proton exchange rate and concentration in chemical exchange saturation transfer imaging of the human brain," *NeuroImage*, vol. 189, 2019.

[24] A. J. Carradat *et al.*, "Measuring chemical exchange saturation transfer exchange rates in the human brain using a particle swarm optimisation algorithm," *NMR in Biomedicine*, vol. 36, no. 11, 2023.

[25] D. M. Blei, A. Kucukelbir, and J. D. McAuliffe, "Variational Inference: A Review for Statisticians," *Journal of the American Statistical Association*, vol. 112, no. 518, pp. 859–877, Apr. 2017.

[26] H. Attias, "A Variational Bayesian Framework for Graphical Models," in *Advances in Neural Information Processing Systems*, vol. 12. MIT Press, 1999.

[27] M. A. Chappell *et al.*, "Variational Bayesian Inference for a Nonlinear Forward Model," *IEEE Trans. Signal Process.*, vol. 57, no. 1, pp. 223–236, Jan. 2009.

[28] D. P. Kingma and M. Welling, "Auto-Encoding Variational Bayes," Dec. 2022.

[29] F. Liu *et al.*, "Magnetic resonance parameter mapping using model-guided self-supervised deep learning," *Magnetic Resonance in Medicine*, vol. 85, no. 6, pp. 3211–3226, 2021.

[30] Y. Jun *et al.*, "SSL-QALAS: Self-Supervised Learning for rapid multi-parameter estimation in quantitative MRI using 3D-QALAS," *Magnetic Resonance in Medicine*, vol. 90, no. 5, pp. 2019–2032, Nov. 2023.

[31] C. Huang *et al.*, "Uncertainty-aware self-supervised neural network for liver T1 $\rho$  mapping with relaxation constraint," *Phys. Med. Biol.*, vol. 67, no. 22, p. 225019, Nov. 2022.

[32] Y. Zhang, J.-Q. Zheng, and M. Chappell, "Bayesian Inference for Non-Linear Forward Model by Using a VAE-Based Neural Network Structure," *IEEE Trans. Signal Process.*, vol. 72, pp. 1400–1411, 2024.

[33] A. Glyn-Davies *et al.*, " $\phi$ -DVAE: Physics-informed dynamical variational autoencoders for unstructured data assimilation," *Journal of Computational Physics*, vol. 515, p. 113293, Oct. 2024.

[34] H. Goh *et al.*, "Solving Bayesian Inverse Problems via Variational Autoencoders," Dec. 2021.

[35] M. A. G. Duff *et al.*, "VAEs with structured image covariance applied to compressed sensing MRI," *Phys. Med. Biol.*, vol. 68, no. 16, p. 165008, Aug. 2023.

[36] Y. Bliesener, J. Acharya, and K. S. Nayak, "Efficient DCE-MRI Parameter and Uncertainty Estimation Using a Neural Network," *IEEE Trans. Med. Imag.*, vol. 39, no. 5, pp. 1712–1723, May 2020.

[37] F. Glang *et al.*, "DeepCEST 3T: Robust MRI parameter determination and uncertainty quantification with neural networks-application to CEST imaging of the human brain at 3T," *Mag. Res. Med.*, vol. 84, no. 1, pp. 450–466, Jul. 2020.

[38] D. Nagar *et al.*, "Dynamic and rapid deep synthesis of chemical exchange saturation transfer and semisolid magnetization transfer MRI signals," *Sci Rep*, vol. 13, no. 1, p. 18291, Oct. 2023.

[39] L. Roussel-Noori *et al.*, "P32-specific car t cells with dual antitumor and antiangiogenic therapeutic potential in gliomas," *Nature communications*, vol. 12, no. 1, p. 3615, 2021.

[40] J. L. Ross *et al.*, "Microglia and monocyte-derived macrophages drive progression of pediatric high-grade gliomas and are transcriptionally shaped by histone mutations," *Immunity*, vol. 57, no. 11, pp. 2669–2687, 2024.

[41] D. Nagar *et al.*, "Multi-contrast generation and quantitative mri using a transformer-based framework with rf excitation embeddings," *Communications Biology*, 2025.

[42] M. Kim *et al.*, "Water saturation shift referencing (wassr) for chemical exchange saturation transfer (cest) experiments," *Magnetic Resonance in Medicine*, vol. 61, no. 6, pp. 1441–1450, 2009.

[43] P. Schuenke *et al.*, "Simultaneous mapping of water shift and b1 (wasabi)—application to field-inhomogeneity correction of cest mri data," *Mag. Res. Med.*, vol. 77, no. 2, pp. 571–580, 2017.

[44] S. Mueller *et al.*, "Whole brain snapshot cest at 3t using 3d-epi: aiming for speed, volume, and homogeneity," *Magnetic resonance in medicine*, vol. 84, no. 5, pp. 2469–2483, 2020.

[45] J. Bradbury *et al.*, "JAX: composable transformations of Python+NumPy programs," *github*, 2018.

[46] B. Kim *et al.*, "A deep learning approach for magnetization transfer contrast mr fingerprinting and chemical exchange saturation transfer imaging," *Neuroimage*, vol. 221, p. 117165, 2020.

[47] D. Paech *et al.*, "Whole-brain intracellular ph mapping of gliomas using high-resolution 31p mr spectroscopic imaging at 7.0 t," *Radiology: Imaging Cancer*, vol. 6, no. 1, p. e220127, 2023.

[48] C. Nilsson *et al.*, "Cytosolic acidification and lysosomal alkalinization during tnf- $\alpha$  induced apoptosis in u937 cells," *Apoptosis*, vol. 11, no. 7, pp. 1149–1159, 2006.

[49] D. L. Raunig *et al.*, "Multiparametric quantitative imaging biomarker as a multivariate descriptor of health: a roadmap," *Academic radiology*, vol. 30, no. 2, pp. 159–182, 2023.

[50] O. Perlman *et al.*, "CEST MR-Fingerprinting: Practical considerations and insights for acquisition schedule design and improved reconstruction," *Magnetic Resonance in Medicine*, vol. 83, no. 2, pp. 462–478, 2020.

## ACKNOWLEDGMENT

The authors thank Tony Stöcker and Rüdiger Stirnberg for their help with the 3D EPI readout. The study was supported in part by Moonshot-Med, a joint grant program from Tel Aviv University and Clalit Innovation, the innovation arm of Clalit Health Services, and the Edmond J. Safra Center for Bioinformatics at Tel Aviv University. This work was supported by the German Research Foundation (DFG, ZA 814/15-1) and the Israel Science Foundation (grant No. 1030/25). A.F. acknowledges the support of the TAD Excellence Program for Doctoral Students in Artificial Intelligence and Data Science. This project was funded by the European Union (ERC, BabyMagnet, project no. 101115639). Views and opinions expressed are, however, those of the authors alone and do not necessarily reflect those of the European Union or the European Research Council. Neither the European Union nor the granting authority can be held responsible for them.